Comparison of Power and Efficiency in Synchronous Converter with INC and P&O MPPT Algorithm

[1]MEAS Saran, [2]AM Sok Chea, [3]KIM Bunthern, [4]CHRIN Phok, [5]NY Virbora, [6]SRIM Saravuth

[1,2,3,4]Energy Technology and Management (ETM), Institute of Technology of Cambodia (ITC), Phnom Penh, Cambodia
[5,6]Faculty of Electronics of National Polytechnic Institute of Cambodia (NPIC), Phnom Penh, Cambodia

Abstract - **A maximum power point tracking (MPPT) algorithm optimizes the power output of a solar panel by continuously adjusting the duty cycle based on real-time voltage and current measurements. This process ensures the system operates at the panel's maximum power point without overloading it. However, maintaining converter stability and fast convergence under varying solar irradiance conditions poses a challenge, as output power can oscillate before stabilizing at the maximum power point. Traditional non-synchronous converters use fast-switching diodes to block reverse current, but in high-current applications, power loss increases significantly due to the diode's internal resistance. Synchronous converters, by using the MOSFET's intrinsic body diode, address this issue and enhance efficiency. This paper focuses on comparing the performance and power conversion efficiency of the two converter types, highlighting the improvements in power extraction and efficiency at the maximum power point.**

Keywords: Bidirectional Converter, Incremental Conductance, MPPT, Non-isolated DC-DC Converter, Perturb and Observe, Synchronous Converter.

I. INTRODUCTION

The challenge of renewable energy is a high priority for many fields, especially energy conversion and energy storage engineering, as solar energy is considered a firmly established energy source technology[1]. A solar panel converts solar radiation from photons, exciting the thin-film silicon semiconductor into an electrical current. However, the electric current produced by the solar panel can greatly vary depending on the solar irradiance and changing temperature [2]. Despite the changing solar irradiance and temperature decreasing the power output as the temperature increases, solar power efficiency changes linearly concerning the changing temperature, despite the nonlinear behavior of the solar power curve [3], [4]. However, solar panels cannot provide the maximum power point on their own without the MPPT algorithm, as the conventional MPPT algorithm, such as the hill-climbing algorithm, can provide a maximum power point under a uniform solar irradiance but is lacking and not

well-adapted to unpredictable changes in temperature and solar irradiances, such as seasonal changes and partial shading, as described in [5]. These conditions pose challenges to the MPPT's stability. The two algorithms, incremental conductance (INC) and perturb and observe (P&O), have a difference in computing speed and steady-state response but guarantee maximum solar power harnessing [6]. The MPPT algorithm alone cannot always ensure maximum power harnessing, since the main role in the power conversion is proposed in a bidirectional boost converter design, as a conventional DC-DC converter can have a lower efficiency [7]. By maximizing the converter efficiency, the power harnessed from the solar panel can stay close to the maximum power point. Parasitic parameters of the semiconductor and RLC components greatly affect both performance and efficiency, as discussed in [8], [9], [10]. In this research, a synchronous bidirectional converter is designed to address this issue by using a high-side MOSFET to replace the conventional fast-switching diode. The 48V 100Ah lead-acid battery is used for energy storage, and the addition of a charging status to the battery is considered. The state of charge (SoC) of the battery can affect the MPPT tracking condition of the algorithm since the first state of the charge cycle of the bulk and absorption stages requires full power to charge the battery. This condition allows full support for an MPPT. The third and fourth states of charge, the floating and equalization, require a low current from the converter to maintain the fully charged voltage [11], [12], [13].

II. LITERATURE REVIEW

The photovoltaic (PV) output power characteristics can be described using (1); the temperature coefficient γ is -0.4% per °C with the standard testing condition at Tstc = 25 °C, the power output Pstc and solar irradiance Gstc[14].

$$P \approx P_{\text{stc}} \left(\frac{G}{G_{\text{stc}}} \right) \left(1 + \gamma (T - T_{\text{stc}}) \right) \qquad (1)$$

Following (1), the output power greatly depends on the solar irradiance, as shown in Figure 1, and the cell's temperature. As the temperature increases, the output power P decreases gradually, as shown in Figure 2.

Table 1: BESUTO 330WP solar panel electrical specification

Parameter	Notation	Value	Unit
Rated Maximum Power	P_{max}	330	W
Output Tolerance	-	±3	%
Voltage at MPPT	V_{MPP}	37.9	V
Current at MPPT	I_{MPP}	8.71	A
Open Circuit Voltage	V_{OC}	45.9	V
Short Circuit Current	I_{SC}	9.16	A

Figure 3 shows the non-linear curve of the output solar power concerning the solar irradiance and changing temperature. The MPPT algorithm ensures the solar panel outputs power at the MPP while maintaining the solar terminal voltage at the VMPP.
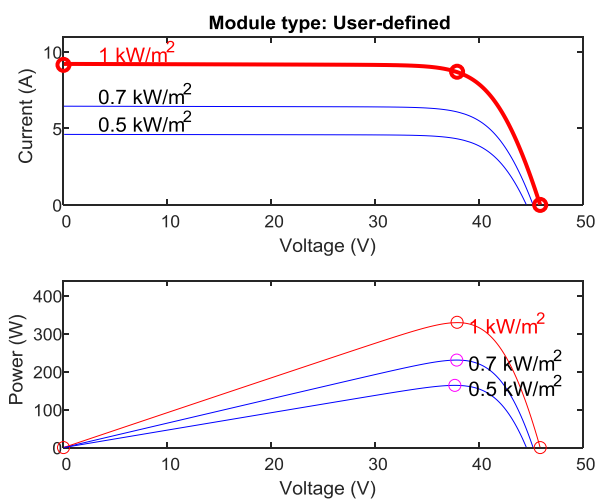
Figure 1: Fixed temperature of 25°C with changing solar irradiance of 500 W/m², 700 W/m², and 1 kW/m²
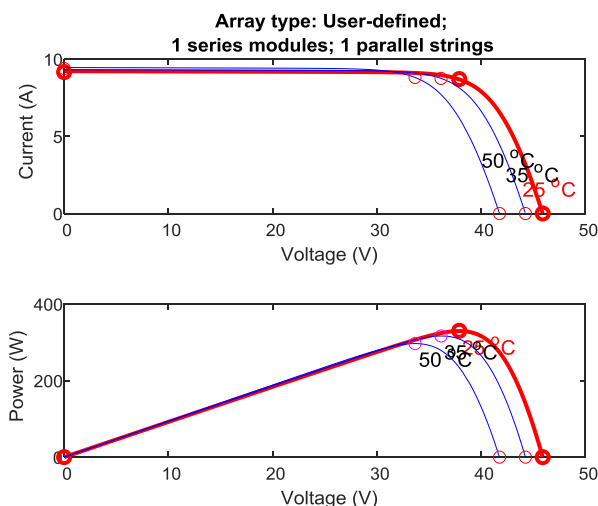
Figure 2: Fixed solar irradiance of 1 kW/m² with changing temperature at 25 °C, 35 °C, and 50 °C

Figure 3 shows the schematic diagram of the bidirectional converter. This converter consists of two N-channel MOSFETs, where Q_1 is the low-side MOSFET, and Q_2 is the high-side MOSFET, which is the MOSFET used for

the fast-switching diode replacement. The VMPP of the solar panel is below the battery's charging voltage, and the boost converter configuration of the bidirectional converter is ideal for this requirement. A step-up converter ensures the charge voltage at a maximum of 57.6 V for the bulk and absorption state of the battery. However, the design challenges arise as the equivalent series resistance (ESR) causes two issues, such as a voltage drop on the inductor at a high-power output and a non-convergence to the design output voltage as the duty cycle increases, opposing the voltage drop on the inductor [15]. Inductor analysis is crucial for the power loss optimization on the magnetic component. The semiconductor switches prove to be a key component for power loss optimization. The bidirectional converter tackles this problem by enhancing the conversion efficiency due to the lower power loss on the switching component, as the MOSFET R_{DS} resistance is generally less than 100 mΩ. At a higher current application, this resistance proves an advantage in hardware design [16], [17]. In contrast, the conventional diode has an increasing forward voltage characteristic following (2); as the forward current increases, so does the power loss.

$$V_d = nV_T \ln\left(\frac{I + I_0}{I_0}\right) \quad (2)$$

A MOSFET and a diode were demonstrated to have linear power loss characteristics; however, in practical applications, the MOSFETs proved to be more efficient than a fast-switching diode due to low internal drain-source resistance, while the high current characteristic is suitable for a high-current application and a smaller footprint design. The lower power dissipation also benefits the converter operating without a heatsink and improves the overall thermal performance compared to a fast-switching diode [18].
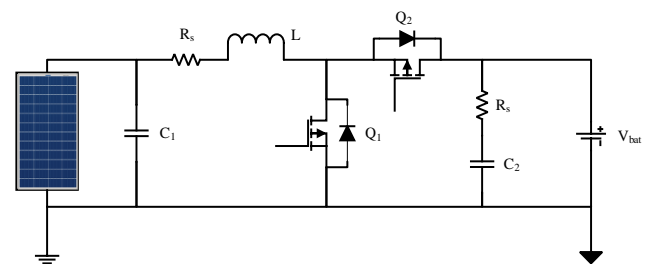

Figure 3: A synchronous bidirectional converter

Figure 4 shows the operation of the bidirectional boost converter. In this state, Q_1 is ON, allowing the current to flow through the inductor and be stored as the magnetic field, while Q_2 is OFF and acts as the reverse bias diode. As the PWM changes are shown inFigure 5, Q_1 is in an OFF state and acts as a reverse bias diode. The energy stored in the inductor is released and flows past Q_2 in the OFF state. In the implementation, the dead time is introduced to both

MOSFETs to prevent the shoot-through connecting the PV and battery from directly shorting to the ground; a good dead time between the ON and OFF states of the PWM could reduce the power losses on the switching cycle [19], [20].
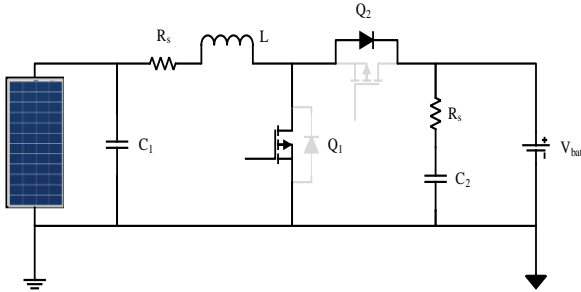

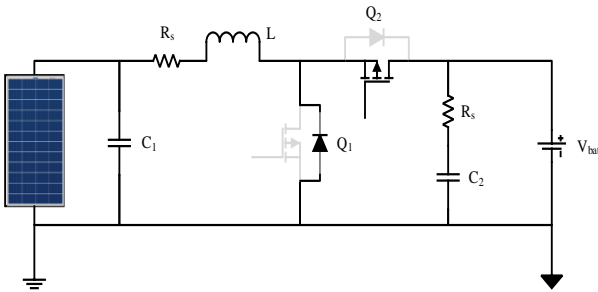**Figure 4: The Q1 is ON and the Q2 is OFF**

Figure 5: The Q1 is OFF and the Q2 is ON

Besides the semiconductor components, the RLC component proves a greater challenge in power loss optimization in hardware design. An inductor forms from a coil; the winding resistance/copper loss could be neglected in an ideal simulation. However, in practical design, winding resistance poses two issues: a higher power loss and a voltage drop at a higher current [21]. The required LC components are calculated using (3) to (5) following a conventional boost converter calculation [13]. The converter design is set to $V_s = V_{\text{MPP}} = 37.9$ V and the output voltage $V_o = 57.6$ V at the switching frequency $F_{sw} = 50$ kHz. The power rating of the converter is set to the P_{MPP} of the PV.

$$D = 1 - \frac{V_s}{V_o} \qquad (3)$$

To provide a steady current output, the continuous conduction mode (CCM) is used in the design for the 40% ripple current.

$$L = \frac{V_s D T}{\Delta i_L} = \frac{V_s D}{\Delta i_L F_{sw}} \qquad (4)$$

The capacitance is designed to provide a ripple voltage of 1 mV.

$$C = \frac{D}{R \left(\frac{\Delta V_o}{V_o}\right) F_{sw}} \qquad (5)$$

The maximum equivalent output capacitor ESR following (6), the value ensures the converter can converge to the desired output voltage without putting the converter into a short circuit as the duty cycle increases to 100 percent.

$$\Delta V_{o,\text{ESR}} = \Delta i_C r_C = I_{L,\text{max}} r_C \qquad (6)$$

Following the calculation, the yield of the inductance is $L \geq 59.55$ µH and the capacitance is $C \geq 544.29$ µF. The measured winding ESR is greater than 10 mΩ, and the design challenge is to minimize the ESR while maintaining the required inductance. This design consideration is crucial since a converter operates in a CCM mode and requires a larger inductance for handling continuous current. The CCM mode can provide a lower conduction loss due to the switching current never falling to zero, which is suitable for high-power application design. The stranded wires are used to lower the equivalent resistance to address this issue. The inductor design is considered to prevent magnetic core saturation; this phenomenon leads to a short circuit. The total power loss on an inductor is the sum of the winding loss and magnetic core loss. The required parameters are calculated following (7) to (9). To select the suitable magnetic core for the design, the magnetic core geometry is selected using:

$$K_g \geq \frac{\rho L_M^2 I_{tot}^2 I_{M,\text{max}}^2}{B_{\text{max}}^2 P_{cu} K_u} 10^8 \qquad (7)$$

The air gap reluctance $\mathfrak{R}_g$ prevents the magnetic core from saturation. The air gap length is calculated using:

$$\ell_g = \frac{\mu_0 L_M I_{M,\text{max}}^2}{B_{\text{max}}^2 A_c} 10^4 \qquad (8)$$

The number of windings:

$$N = \frac{L_M I_{M,\text{max}}}{B_{\text{max}} A_c} \qquad (9)$$

These calculations yield a requirement for a magnetic core with a $K_g \leq 0.218441$ cm^5. The ferrite magnetic core PQ32 is suitable for this requirement, with a required air gap of 850 µm and a winding turn of 16.18 turns. The ferrite magnetic core is selected for a suitable frequency at 50 kHz due to a relatively low core loss compared to the iron-powdered core from 50 to 300 mW/cm³[22], [23].
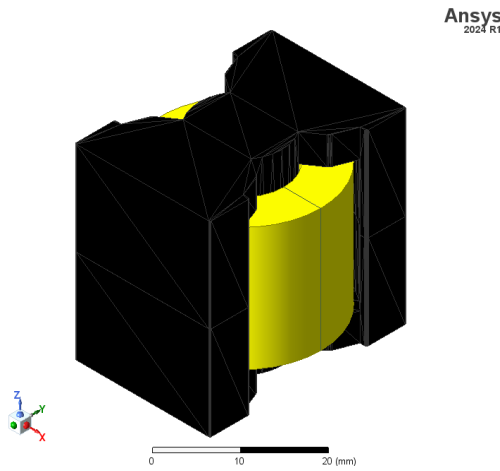
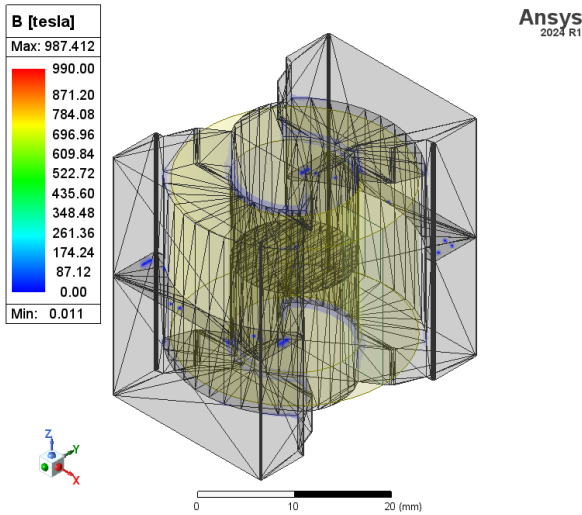**Figure 6: The 3D model of the PQ32 magnetic core in ANSYS Maxwell**

Figure 7: Visualizing the magnetic flux density in the parts of the ferrite core

Figure 7 visualizes the magnetic flux density of the ferrite core. In most applications, the saturation magnetic flux density is $B_{sat} \leq 0.5$ T. The simulation results show that the magnetic core operates without saturation, ensuring lower power loss on the magnetic core, and only peaks at a small region of the magnetic core [24]. Figure 8 is the perturb and observe algorithm. This algorithm measures the real-time PV's voltage and current and operates on the changes in solar power. If the perturbed power is increased, so is the duty cycle; otherwise, the duty cycle is increased. This algorithm is simple in both algorithm design and computational perspective. Figure 9is the incremental conductance algorithm. This algorithm has a condition to measure if the MPP is reached by comparing the equality of $I = -V \times \frac{\Delta I}{\Delta V}$; otherwise, the algorithm increases the duty cycle as the $I < -V \times \frac{\Delta I}{\Delta V}$ and decrease the duty cycle as $I > -V \times \frac{\Delta I}{\Delta V}$. This comparison shows a significant difference between the INC and P&O algorithms; the INC can compute MPP, while P&O is lacking [25], [26].
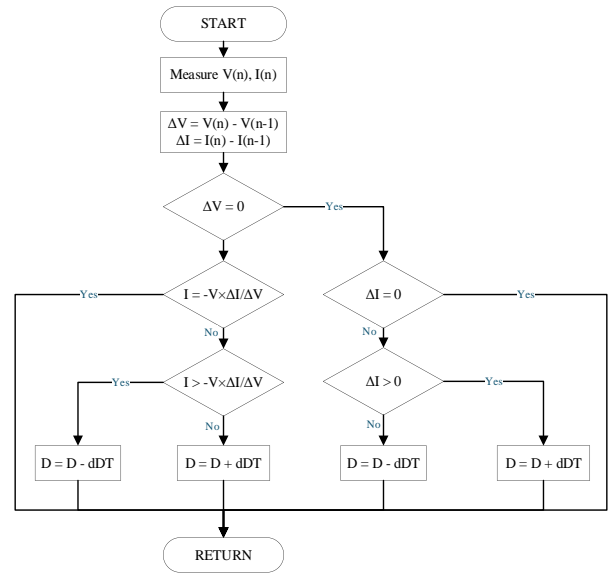
Figure 8: The incremental conductance algorithm
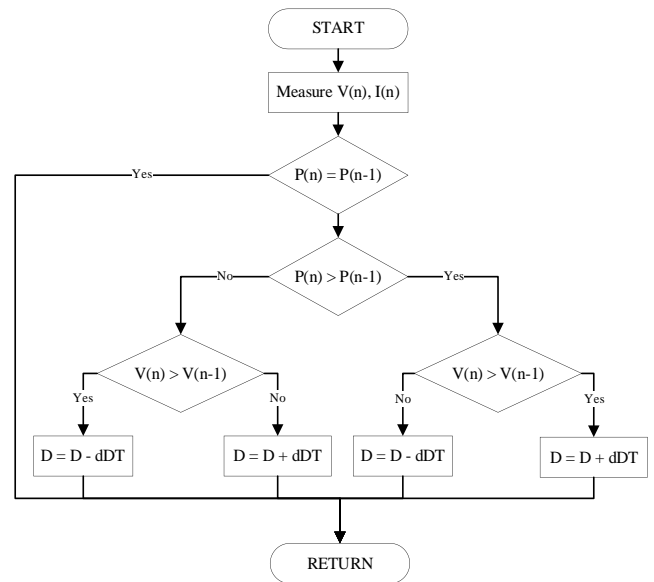
Figure 9: The perturb and observe algorithm

III. METHODOLOGY

The methodology section was divided into battery and MPPT algorithm simulation and, ultimately, the hardware experimentation. The battery's characteristics simulation was conducted in the Simulink environment. The lead-acid battery was selected with a 48 V 100 Ah. The dynamic response of the battery is shown in Figure 11and Figure 12. The graph is represented as voltage and current discharge over time, showing the visualization of the battery's SoC.
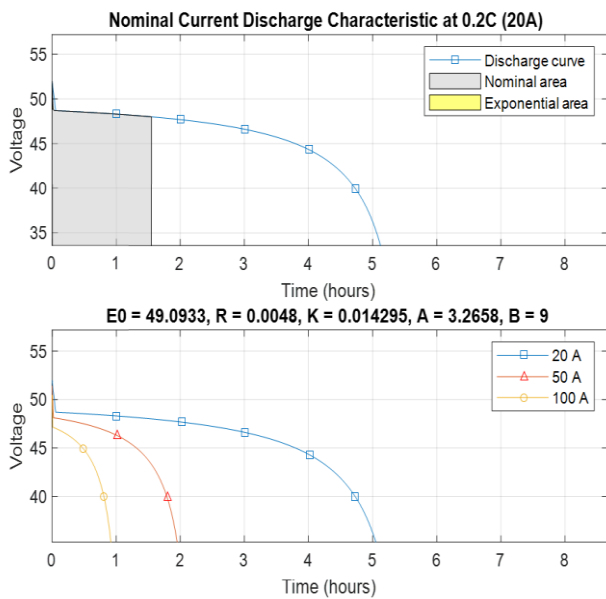
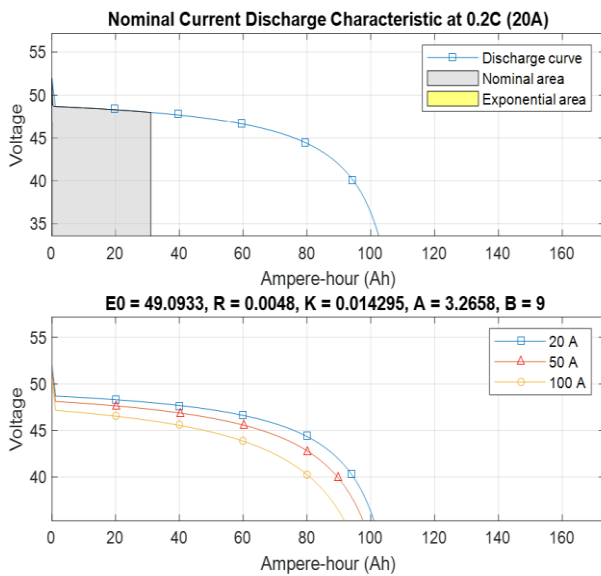**Figure 10: The dynamic response of the battery over time**

Figure 11: The total charge delivered over time

The INC and P&O algorithms were implemented from the Figure 8 and Figure 9 diagrams and simulated with four different battery SoCs, as shown in Figure 16 to Figure 19. In this simulation, the MPP of the solar panel was set at 330 W, following the PV electrical parameters from Table 1 with solar irradiance of 1000 W/m²at 25°C. In Figure 13, the assembled bidirectional boost converter is connected to the solar panel and the lead-acid battery, along with the microcontroller and hardware components.
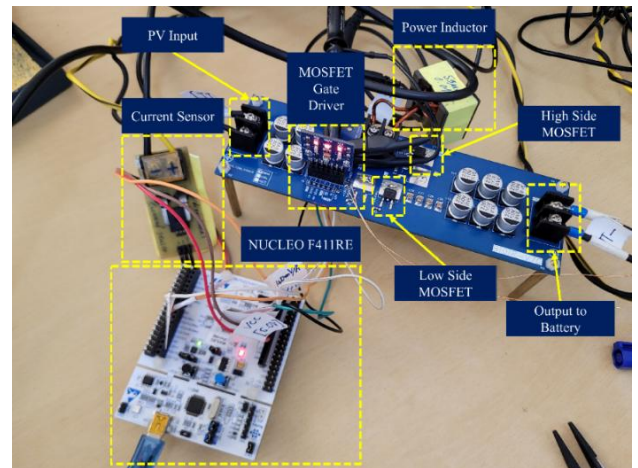
Figure 12: The bidirectional boost converter hardware assembly

The hardware components and measuring instruments used in the experiments are listed in Table 2 and Table 3. The controlled PWM signal is generated by the STM32 TIM3 CH1 at 50 kHz to the half-bridge gate driver. Figure 14 and Figure 15 demonstrate that the synchronous output signal from the gate driver has a dead time of ~330 ns. This signal allows the MOSFETs to operate without cross conductance, which can lead to the converter's short-circuit condition.

Table 2: The microcontroller and hardware components

Hardware	Model Number
Microcontroller	NUCLEO-STM32F411RE
Bidirectional hall-effect current sensor	ACS758LCB-050U-PFF-T
Half-bridge gate driver	2ED2104S06F
Ferrite magnetic core	PQ-32

Table 3: The measuring instruments

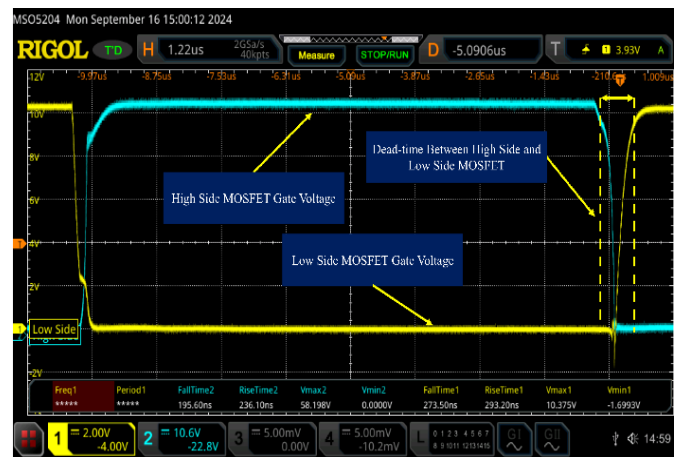| Hardware	Model Number
Digital oscilloscope	RIGOL MSO5204
Oscilloscope probe	RIGOL RP3500A
Digital multimeter	Fluke 17B+

Figure 13: The implemented deadtime on the high-side and low-side of the MOSFET
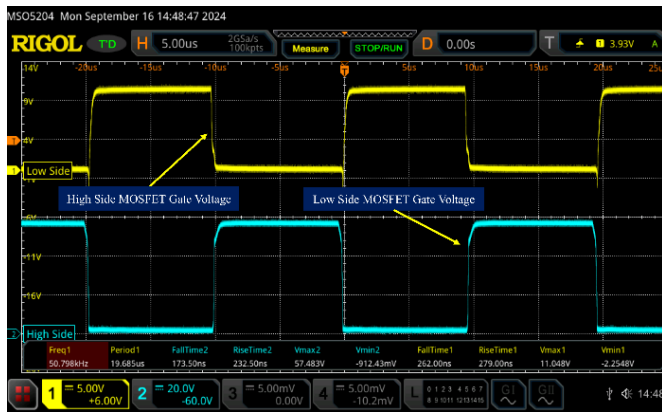
Figure 14: Operational PWM signal during MPP

The simulation testing with the MPPT for the first stage involved the different batteries at 25%, 50%, 75%, and 100% SoC. This testing condition is set to a fixed solar irradiance of 1000 W/m²at 25℃, later discussed from Figure 16 to Figure 19 and from Figure 20 to Figure 23. The second stage simulation is tested with the changing solar irradiance of 500 W/m², 700 W/m², 1000 W/m², and back to 500 W/m² at a fixed temperature of 25℃, as discussed in Figure 15 to Figure 18 and Figure 19 to Figure 22. The hardware experimentation was conducted with the assembled hardware, with a testing period of 30 minutes while charging the battery at a 10% SoC with ambient temperature around 35℃ to 40℃.

IV. RESULTS AND DISCUSSION

Figure 15 demonstrates the ability of the INC algorithm to converge to the PV's MPP, while the P&O algorithm failed to converge, staying at a much lower MPP. However, the P&O has a more stable power ripple at the MPP. As the battery's SoC is set at 100%, Figure 18, the P&O algorithm has a higher MPP close to the PV's MPP compared to Figure 15.
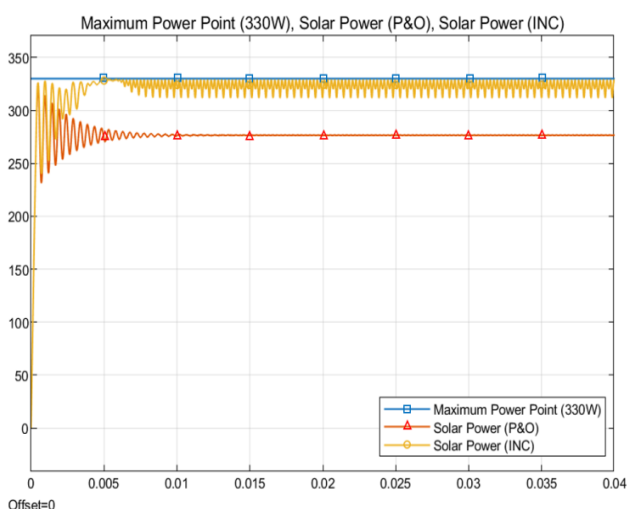
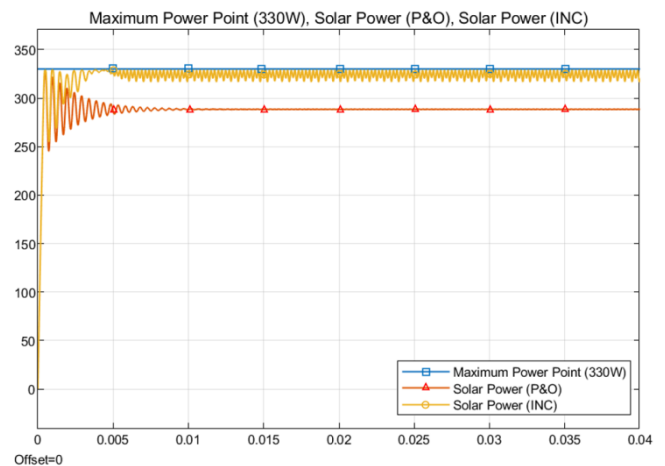**Figure 15: Simulated condition with the battery's 25% SoC**

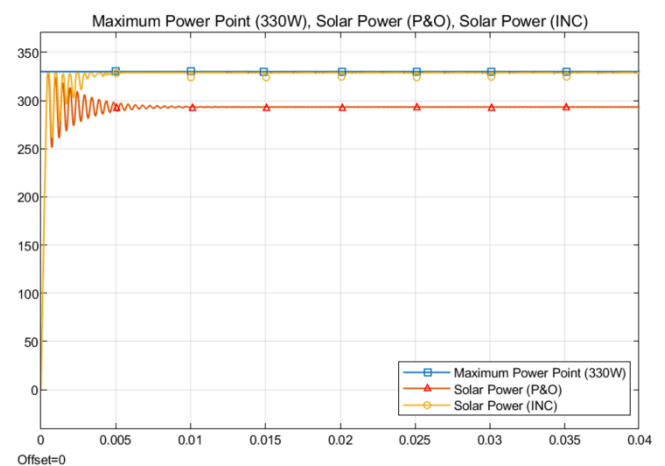**Figure 16: Simulated condition with the battery's 50% SoC**

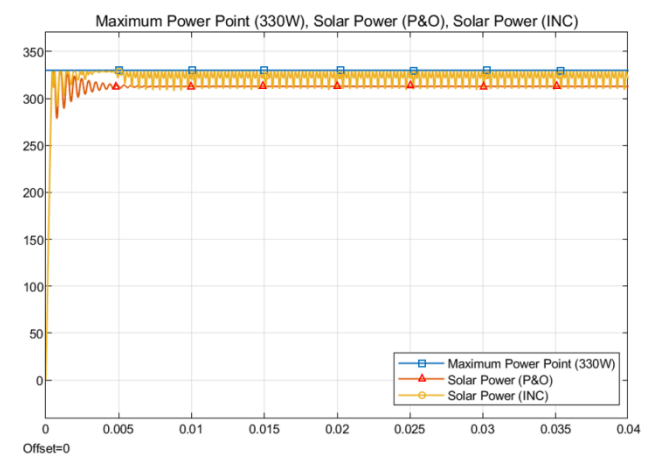**Figure 17: Simulated condition with the battery's 75% SoC**

Figure 18: Simulated condition with the battery's 100% SoC

Following the simulation, the comparison between the INC and P&O algorithms and the ability to track the MPP showed that, despite using the same step size dDT, the P&O algorithm failed to converge with the MPP and was stuck at the local maxima. This condition is caused by oscillation when the algorithm reaches near the PV's MPP and leads to

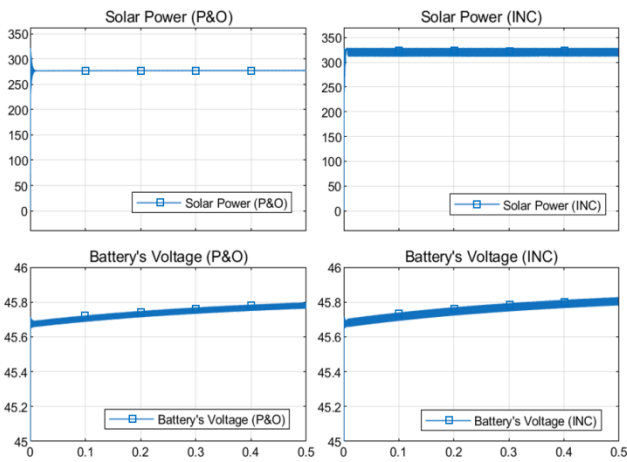incorrect readings, mistakenly settling at a lower power point [27].

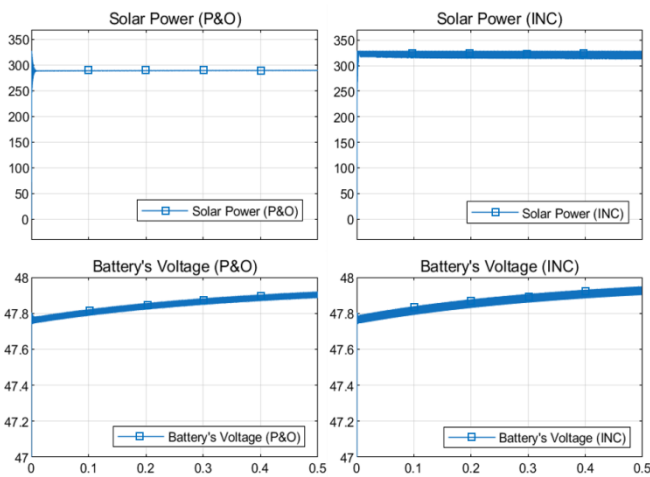**Figure 19: Simulated condition with the battery's 25% SoC**

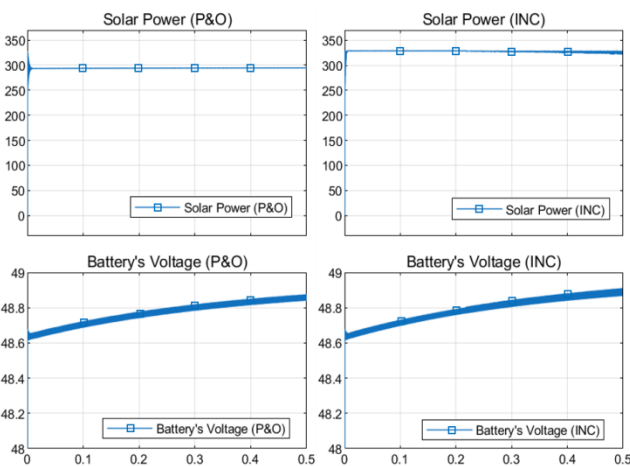**Figure 20: Simulated condition with the battery's 50% SoC**

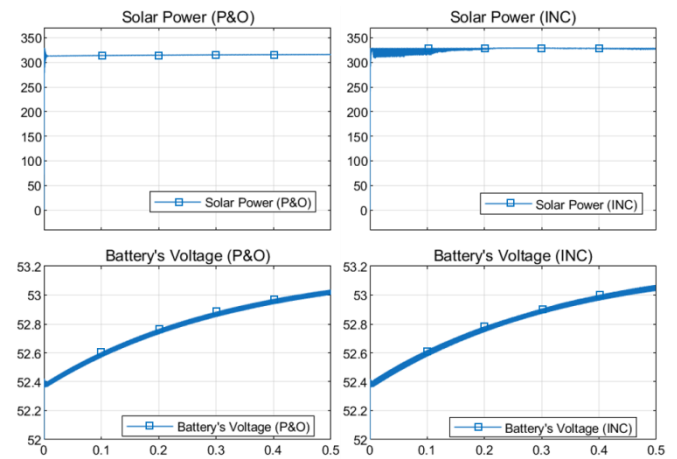**Figure 21: Simulated condition with the battery's 75% SoC**

Figure 22: Simulated condition with the battery's 100% SoC

The increasing battery voltage is simulated in different SoCs, as shown in Figure 19 to Figure 22. In these simulations, observe the power obtained from PV and the charging battery's voltage. In Figure 19, the INC and P&O charging algorithms provide power to the battery at 25% SoC. At this state, the voltage comparison between the algorithms doesn't significantly differ. However, as the SoC increases, the INC has better performance at converging to the MPP. This algorithm also provides a faster charging speed for the battery's voltage.
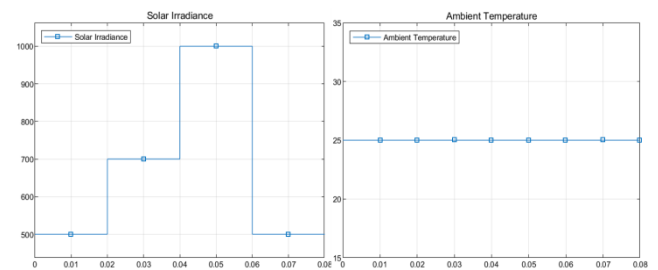

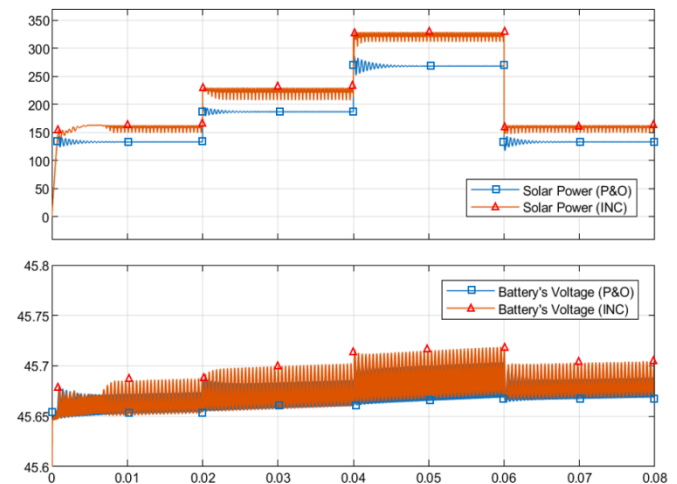**Figure 23: The changing solar irradiance and fixed PV temperature**
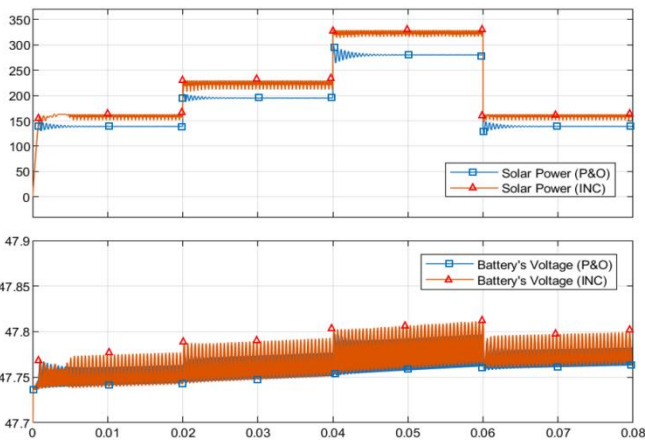

Figure 24: Simulated condition with the battery's 25% SoC

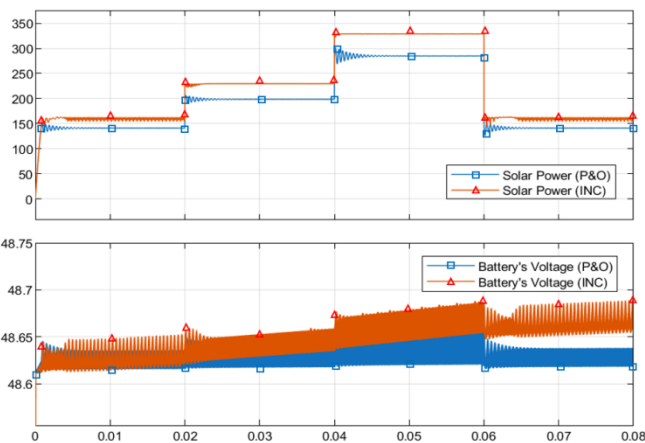**Figure 25: Simulated condition with the battery's 50% SoC**

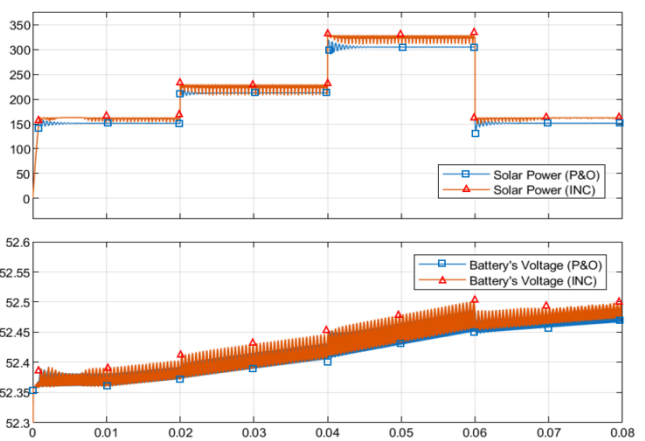**Figure 26: Simulated condition with the battery's 75% SoC**

Figure 27: Simulated condition with the battery's 100% SoC

Figure 24 to Figure 27 shows the transient performance comparison between the INC and P&O algorithms. Following Figure 24 and Figure 25, the transient of the MPP at the first 10 seconds with hardware implementation is shown. However, the first few seconds show a similar linear characteristic. This condition is due to the soft start implementation to prevent the inrush current during start-up. Figure 26 shows both algorithms' MPP transient responses; both algorithms can

achieve a very similar MPPT performance; however, the INC algorithm can obtain a higher power while this testing condition maintains the same battery's SoC and solar irradiance. The INC algorithm proves to have faster MPPT performance than the P&O algorithm, maintaining a lower PV voltage oscillation and a more stable VPP, as shown in Figure 27.
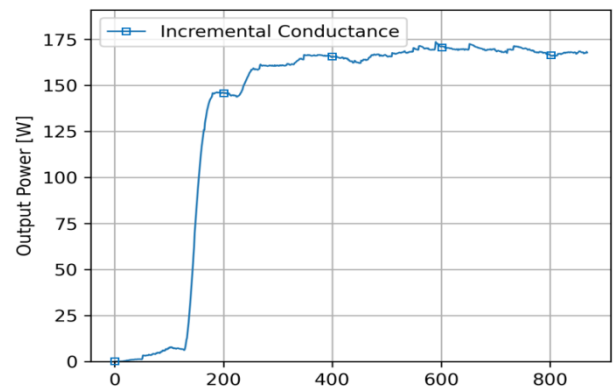

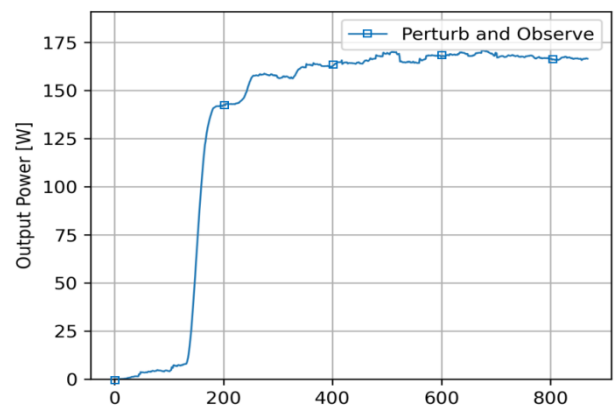**Figure 28: MPP transient response of the INC algorithm with 10% battery SoC**

Figure 29: MPP transient response of the P&O algorithm with 10% battery SoC
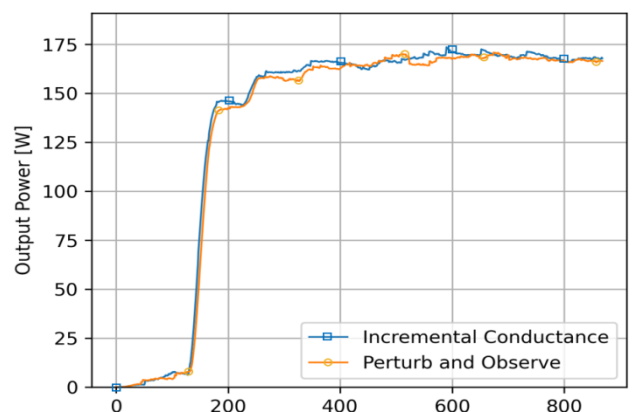

Figure 30: MPP transient response comparison between INC and P&O algorithm with 10% battery SoC
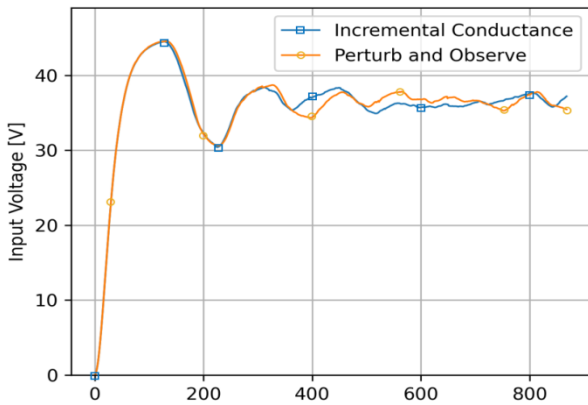
Figure 31: MPP voltage transient response comparison between INC and P&O algorithm with 10% battery SoC

The following results were collected from the 30-minute experiments. The battery was charging at 10% SoC and 46 V and changed solar irradiance. Figure 32 and Figure 34 demonstrated a significant difference between the INC and P&O algorithms with changing solar irradiance compared to the transient response from Figure 28 to Figure 31.

Table 4: The INC and P&O algorithms' MPP characteristics comparison

Algorithm	Actual P_{MPP} vs Solar P_{MPP} (%)	Actual V_{PP} vs Solar V_{PP} (%)
Incremental conductance	97.36	97.15
Perturb and observe	90.91	63.35

In the first 12 minutes, the P&O algorithm in Figure 36can obtain only close to 90.91% MPP; however, the PV's voltage is 37% lower than the PV's VPP compared to the INC algorithm at 97.36% in Figure 39. These experiments agreed with the Simulink simulation model from Figure 15 to Figure 18. As the solar irradiance changed, the P&O algorithm tended to fail to continue the MPPT after the change in solar irradiance in Figure 39; at this condition, the PV's voltage had gone back to the PV's VOC. In Figure 39, the INC algorithm can continue obtaining the MPP during the lower solar irradiance. This implies the voltage drops at the charging voltage shown in Figure 34 and Figure 38.
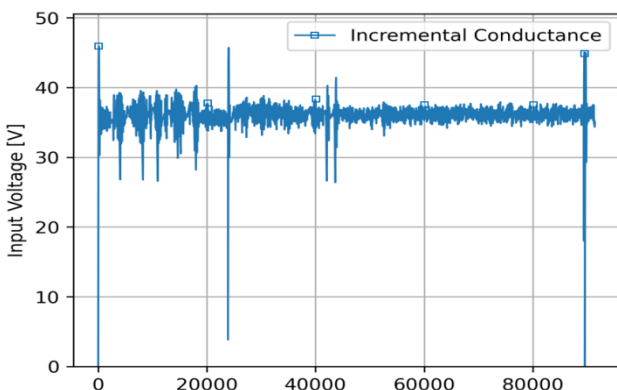

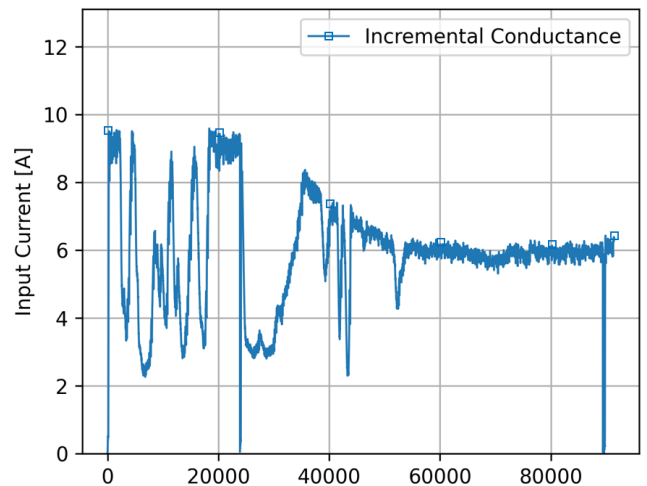**Figure 32: The changing PV's voltage during MPPT**

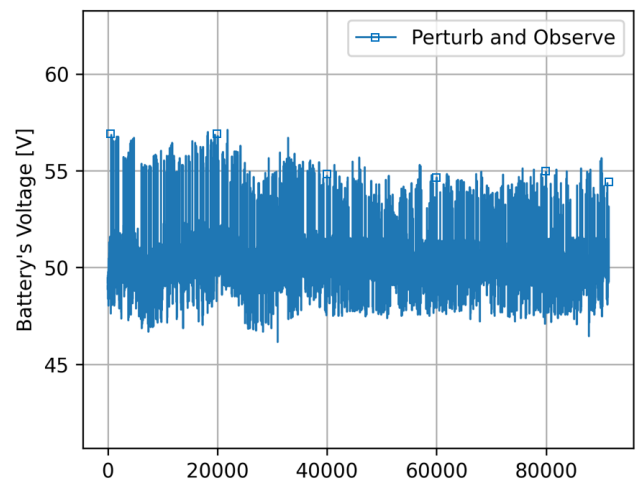**Figure 33: The changing PV's current during MPPT**

Figure 34: The changing battery's voltage during MPPT

Figure 35: The changing solar power during MPPT
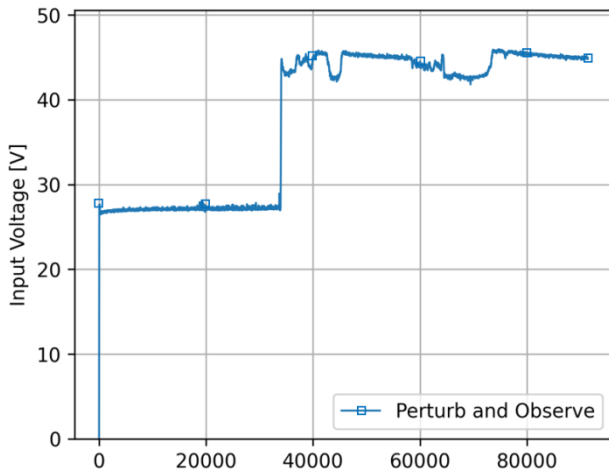
Figure 36: The changing PV's voltage during MPPT

Figure 37: The changing PV's current during MPPT

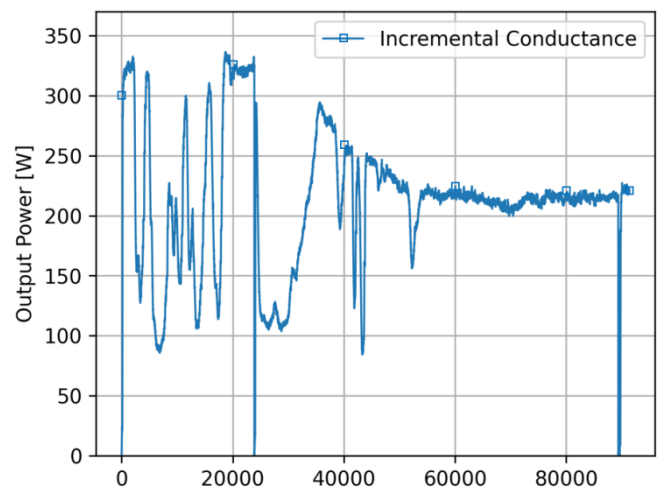
Figure 38: The changing battery voltage during MPPT

Figure 39: The changing solar power during MPPT

Table 5: The average synchronous converter efficiency comparison

Algorithm	Average efficiency (%)
Incremental conductance (INC)	97.65%
Perturb and observe (P&O)	96.97%

Figure 39 shows the MPPT with the P&O algorithm; however, the maximum power obtained on average is around 300 W. As the battery is at 46 V, both algorithms can boost the VMPP to around 50 V. Figure 41 shows that the P&O algorithm can boost the VPP to the output voltage around 3% higher than the INC algorithm. However, the significant drawback is the failure to obtain the maximum MPPT and a much lower VPP compared to the INC algorithm.

Figure 40: INC algorithm's voltage charging the battery
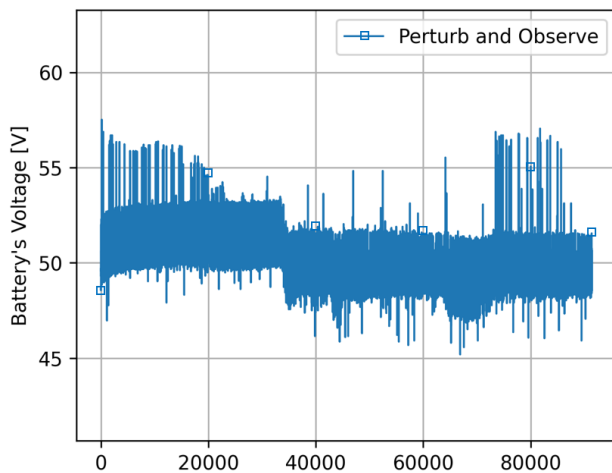
Figure 41: P&O algorithm's voltage charging of the battery

V. CONCLUSION

The implemented experiment, along with the simulation model, demonstrates that the INC algorithm performs better than the P&O algorithm under changing solar irradiance conditions. During the transient response, the INC algorithm achieves a faster MPPT convergence speed than the P&O algorithm. Additionally, during this phase, the INC algorithm exhibits significantly lower VPP oscillation compared to the P&O algorithm. In the hardware implementation, as the solar irradiance frequently fluctuates, the INC algorithm can maintain the MPPT, charging the battery at a stable output voltage. While the P&O algorithm fails to achie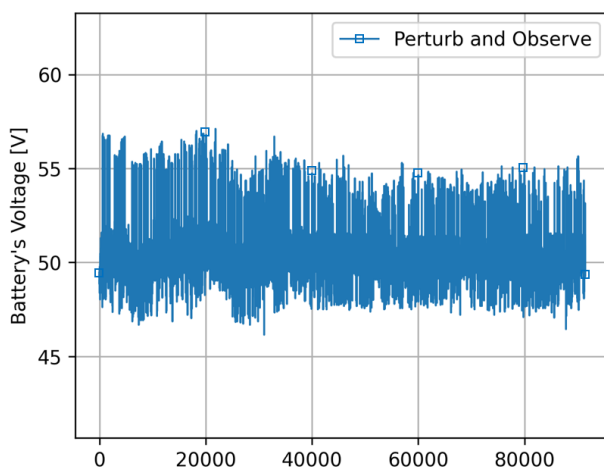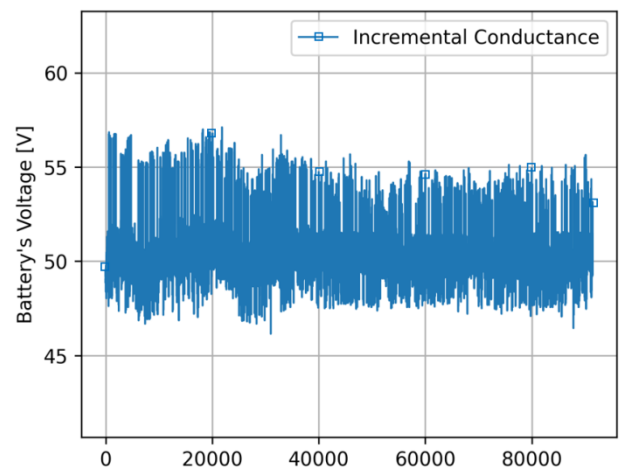ve the MPPT, it can maintain an output voltage close to that of the INC algorithm. This demonstrates that the P&O algorithm failed to obtain the MPP. At peak performance, the INC algorithm reaches the MPP at 97.36%, whereas the P&O algorithm achieves only 90.91% of the rated MPP. Furthermore, applying the INC algorithm with the synchronous converter not only enhances MPPT accuracy but also improves overall energy conversion efficiency by reducing power losses associated with conventional fast-switching diodes. The converter's efficiency can reach up to 97.65% for the implementation with the INC algorithm and 96.97% for the P&O. This is particularly beneficial in high-power applications, where synchronous converters are more suitable for minimizing energy losses and increasing system efficiency.

FUTURE WORK

Further research could focus on improving the adaptation of MPPT algorithms in response to changing solar irradiance. Additionally, investigating methods to reduce VPP oscillations during transient responses could optimize overall output power stability and enhance battery health, especially by facilitating faster charging capabilities.

REFERENCES

[1] H. H. Pourasl, R. V. Barenji, and V. M. Khojastehnezhad, "Solar energy status in the world: A comprehensive review," *Energy Reports*, vol. 10, pp. 3474–3493, Nov. 2023, doi: 10.1016/J.EGYR.2023.10.022.

[2] K. S. Ong, L. Jiang, and K. C. Lai, "Thermoelectric Energy Conversion," *Comprehensive Energy Systems: Volumes 1-5*, vol. 4, pp. 794–815, Jan. 2018, doi: 10.1016/B978-0-12-809597-3.00433-8.

[3] E. Skoplaki and J. A. Palyvos, "On the temperature dependence of photovoltaic module electrical performance: A review of efficiency/power correlations," *Solar Energy*, vol. 83, no. 5, pp. 614–624, May 2009, doi: 10.1016/J.SOLENER.2008.10.008.

[4] N. Fraidenraich and O. C. Vilela, "Performance of solar systems with non-linear behavior calculated by the utilizability method: application to PV solar pumps," *Solar Energy*, vol. 69, no. 2, pp. 131–137, Jan. 2000, doi: 10.1016/S0038-092X(00)00050-5.

[5] N. A. Kamarzaman and C. W. Tan, "A comprehensive review of maximum power point tracking algorithms for photovoltaic systems," *Renewable and Sustainable Energy Reviews*, vol. 37, pp. 585–598, Sep. 2014, doi: 10.1016/J.RSER.2014.05.045.

[6] S. Guo, R. Abbassi, H. Jerbi, A. Rezvani, and K. Suzuki, "Efficient maximum power point tracking for a photovoltaic using hybrid shuffled frog-leaping and pattern search algorithm under changing environmental conditions," *J Clean Prod*, vol. 297, p. 126573, May 2021, doi: 10.1016/J.JCLEPRO.2021.126573.

[7] A. Hussain, R. Akhtar, B. Ali, S. E. Awan, and S. Iqbal, "A Novel Bidirectional DC–DC Converter with Low Stress and Low Magnitude Ripples for Stand-Alone Photovoltaic Power Systems," *Energies 2019, Vol. 12, Page 2884*, vol. 12, no. 15, p. 2884, Jul. 2019, doi: 10.3390/EN12152884.

[8] F. Mumtaz, N. Zaihar Yahaya, S. Tanzim Meraj, B. Singh, R. Kannan, and O. Ibrahim, "Review on non-isolated DC-DC converters and their control techniques for renewable energy applications," *Ain Shams Engineering Journal*, vol. 12, no. 4, pp. 3747–3763, Dec. 2021, doi: 10.1016/J.ASEJ.2021.03.022.

[9] D. G and S. N. Singh, "Selection of non-isolated DC-DC converters for solar photovoltaic system," *Renewable and Sustainable Energy Reviews*, vol. 76, pp. 1230–1247, Sep. 2017, doi: 10.1016/J.RSER.2017.03.130.

[10] T. Sutikno, R. A. Aprilianto, and H. S. Purnama, "Application of non-isolated bidirectional DC–DC converters for renewable and sustainable energy systems: a review," *Clean Energy*, vol. 7, no. 2, pp. 293–311, Apr. 2023, doi: 10.1093/CE/ZKAC070.

[11] D. Calasanzio, M. Maja, and P. Spinelli, "Fast charging of lead/acid batteries," *J Power Sources*, vol. 46, no. 2–3, pp. 375–381, Oct. 1993, doi: 10.1016/0378-7753(93)90033-W.

[12] V. Salas, E. Olías, A. Barrado, and A. Lázaro, "Review of the maximum power point tracking algorithms for stand-alone photovoltaic systems," *Solar Energy Materials and Solar Cells*, vol. 90, no. 11, pp. 1555–1578, Jul. 2006, doi: 10.1016/j.solmat.2005.10.023.

[13] Daniel W. Hart, "Power Electronics." Accessed: Oct. 12, 2024. [Online]. Available: https://www.mhprofessional.com/power-electronics-9780073380674-usa

[14] John A. Duffie and William A. Beckman, "Solar Radiation," *Solar Engineering of Thermal Processes*, pp. 3–42, Apr. 2013, doi: 10.1002/9781118671603.CH1.

[15] V. Ny, S. Meas, and C. Srun, "Implementation of Synchronous Bidirectional Converter Using a Fuzzy Logic Controller," *Journal of Electrical and Electronic Engineering 2023, Volume 11, Page 99*, vol. 11, no. 5, pp. 99–114, Sep. 2023, doi: 10.11648/J.JEEE.20231105.11.

[16] George Lakkas, "Enterprise Systems Analog Applications Journal MOSFET power losses and how they affect power-supply efficiency," *"Analog Application Journal,"* pp. 22–26, 2016.

[17] I. C. Guran, A. Florescu, and L. A. Perișoară, "A Novel ON-State Resistance Modeling Technique for MOSFET Power Switches," *Mathematics 2023, Vol. 11, Page 72*, vol. 11, no. 1, p. 72, Dec. 2022, doi: 10.3390/MATH11010072.

[18] I. N. Jiya and R. Gouws, "Overview of Power Electronic Switches: A Summary of the Past, State-of-the-Art and Illumination of the Future," *Micromachines 2020, Vol. 11, Page 1116*, vol. 11, no. 12, p. 1116, Dec. 2020, doi: 10.3390/MI11121116.

[19] P. Amaral, C. Duarte, and P. Costa, "On the impact of timer resolution in the efficiency optimization of synchronous buck converters," *International Journal of Power Electronics and Drive Systems*, vol. 6, no. 4, pp.

693–702, Dec. 2015, doi: 10.11591/IJPEDS.V6.I4.PP693-702.

[20] W. Qiu, S. Mercer, Z. Liang, and G. Miller, "Driver deadtime control and its impact on system stability of synchronous Buck voltage regulator," *IEEE Trans Power Electron*, vol. 23, no. 1, pp. 163–171, Jan. 2008, doi: 10.1109/TPEL.2007.911784.

[21] I. N. Jiya and R. Gouws, "Overview of Power Electronic Switches: A Summary of the Past, State-of-the-Art and Illumination of the Future," *Micromachines 2020, Vol. 11, Page 1116*, vol. 11, no. 12, p. 1116, Dec. 2020, doi: 10.3390/MI11121116.

[22] W. G. Hurley and W. H. Wölfle, "Transformers and Inductors for Power Electronics: Theory, Design and Applications," *Transformers and Inductors for Power Electronics: Theory, Design and Applications*, Mar. 2013, doi: 10.1002/9781118544648.

[23] Ray Ridley and A. Nace, "Modeling Ferrite Core Losses," *"Switching Power Magazine,"* 2006.

[24] R. W. Erickson and D. Maksimović, "Fundamentals of Power Electronics," *Fundamentals of Power Electronics*, 2020, doi: 10.1007/978-3-030-43881-4.

[25] D. P. Hohm and M. E. Ropp, "Comparative study of maximum power point tracking algorithms using an experimental, programmable, maximum power point tracking test bed," *Conference Record of the IEEE Photovoltaic Specialists Conference*, vol. 2000-January, pp. 1699–1702, 2000, doi: 10.1109/PVSC.2000.916230.

[26] T. Esram and P. L. Chapman, "Comparison of photovoltaic array maximum power point tracking techniques," *IEEE Transactions on Energy Conversion*, vol. 22, no. 2, pp. 439–449, Jun. 2007, doi: 10.1109/TEC.2006.874230.

[27] A. N. M. Mohammad, M. A. M. Radzi, N. Azis, S. Shafie, and M. A. A. M. Zainuri, "An Enhanced Adaptive Perturb and Observe Technique for Efficient Maximum Power Point Tracking Under Partial Shading Conditions," *Applied Sciences 2020, Vol. 10, Page 3912*, vol. 10, no. 11, p. 3912, Jun. 2020, doi: 10.3390/APP10113912.

AUTHORS BIOGRAPHY

MEAS Saran is currently enrolled in ITC in Phnom Penh, Cambodia, as a Ph.D. candidate in energy technology and management. A Bachelor of Technology in Electrical Engineering from the National Polytechnic Institute of Cambodia (NPIC) in 2009 and an MSc in Electrical and Electronics Engineering with a focus on Power Electronics from JEONJU University (JJ) in South Korea in 2013. He currently serves as adviser to NPIC's Power Electronics and EVs Lab and deputy chair of the electronic faculty. You can reach him by email at: saranagoldd@gmail.com

AM Sok Chea is the principal supervisor and deputy head of electrical and energy and a project coordinator of energy technology and management at the Institute of Technology of Cambodia. He can be contacted atemail: sokchea_am@itc.edu.kh

KIM Bunthern is a coordinator of the master's program of Energy Technology and Management at the Institute of Technology of Cambodia. Toulouse INP Doctor of Philosophy (PhD) in Electrical and Electronics Engineering2014–2019 Activities and societies: LAPLACE laboratory. Topic of research: Contribution to the design and control of a hybrid renewable energy generation system based on the reuse of electrical and electronics components for rural electrification in developing countries. He can be contacted at email: kimbunthern@itc.edu.kh

CHRIN Phok is the vice dean and head of electrical and energy and a coordinator of the Ph.D. program of energy technology and management at the Institute of Technology of Cambodia. He can be contacted at email: pchrin@itc.edu.kh

NY Virbora has an M.Sc. Tech. in electrical engineering from the National Polytechnic Institute of Cambodia, Phnom Penh, Cambodia, in 2024. He is currently a lecturer in the college of electronics, and his research interests are power electronics, control systems, embedded systems, and artificial intelligence. He can be contacted at email: nyvirakbora@gmail.com

SRIM Saravuth has an M.Sc. in Electrical Engineering from the National Polytechnic Institute of Cambodia in Phnom Penh, awarded in 2024. He is currently a lecturer at the Faculty of Electronics, with a research focus on power electronics. He can be contacted by email at:srimsaravuth@gmail.com

---

Citation of this Article:

MEAS Saran, AM Sok Chea, KIM Bunthern, CHRIN Phok, NY Virbora, & SRIM Saravuth. (2025). Comparison of Power and Efficiency in Synchronous Converter with INC and P&O MPPT Algorithm. *International Research Journal of Innovations in Engineering and Technology - IRJIET*, 9(8), 31-43. Article DOI https://doi.org/10.47001/IRJIET/2025.908005

****